Biomaterials

3D printing of hydroxyapatite scaffolds with good mechanical and biocompatible properties by digital light processing

Yong Zeng[1,2] (iD), Yinzhou Yan[1] (iD), Hengfeng Yan[2,3] (iD), Chunchun Liu[1,2] (iD), Peiran Li[1,2] (iD), Peng Dong[2,4] (iD), Ying Zhao[4] (iD), and Jimin Chen[1,2,*] (iD)

[1] Institute of Laser Engineering, Beijing University of Technology, Beijing 100124, China
[2] Beijing Engineering Research Center of 3D Printing for Digital Medical Health, Beijing University of Technology, Beijing 100124, China
[3] College of Applied Sciences, Beijing University of Technology, Beijing 100124, China
[4] Capital Aerospace Machinery Company, Beijing 100076, China

ABSTRACT

Hydroxyapatite is a scaffold material widely used in clinical repair of bone defects, but it is difficult for traditional methods to make customized artificial bone implants with complicated shapes. 3D printing biomaterials used as personalized tissue substitutes have the ability to promote and enhance regeneration in areas of defected tissue. The present study aimed at demonstrating the capacity of one 3D printing technique, digital light processing (DLP), to produce HA scaffold. Using HA powder and photopolymer as raw materials, a mixture of HA mass ratio of 30 wt% was prepared by viscosity test. It was used for forming ceramic sample by DLP technology. According to differential scanning calorimetry and thermal gravity analysis, it was revealed that the main temperature range for the decomposition of photopolymer was from 300 to 500 °C. Thus, the two-step sintering process parameters were determined, including sintering temperature range and heating rate. XRD analysis showed that the phase of HA did not change after sintering. SEM results showed that the grain of the sintered ceramic was compact. The compression model was designed by finite element analysis. The mechanical test results showed that the sample had good compression performance. The biological properties of the scaffold were determined by cell culture in vitro. According to the proliferation of cells, it was concluded that the HA scaffold was biocompatible and suitable for cell growth and proliferation. The experimental results show that the DLP technology can be used to form the ceramic scaffold, and the photopolymer in the as-printed sample can be removed by proper high-temperature sintering. The ceramic parts with good compression performance and biocompatibility could be obtained.

Address correspondence to E-mail: jimin@bjut.edu.cn

Springer

Introduction

Hydroxyapatite (HA) is a major constituent of hard tissues such as bone and teeth. It has good biodegradable, osteoconductive and biocompatibility, and is considered as an ideal material for implement bone tissue regeneration [1–4]. It is widely used in the tissue engineering and repair of bone defect. The intricate design of artificial bone implant poses high demands on the molding process of bioceramic. Synthetic HA is therefore of great interest as a transplant material to replace tissues [5–10]. While the use of HA in unloaded implants and dental implants is common, the poor mechanical properties of HA do not allow its use in load-bearing implants. 3D printing technology can enable the fabrication of complex and controllable architectures with pre-defined shapes using computer-aided design/computer-aided manufacturing (CAD/CAM). A lot of 3D printing methods have been used to fabricate complex- and delicate-shaped ceramic parts. Selective laser sintering (SLS) of ceramic powder is a kind of ceramic printing technology which has been widely studied [11–14]. It could be shown that SLS ceramic parts are in a state comparable to a biscuit-fired porcelain body. However, due to the existence of residual thermal stress induced by the laser processing, with about half the mechanical strength than a conventional biscuit-fired sample [11]. And the relative density for SLS ceramic samples is usually low. These shortcomings greatly limit the use of SLS ceramic products. Fused deposition modeling (FDM) is another potential method of ceramic 3D printing. Abdullah et al. [15] evaluated the mechanical and physical properties of highly ceramic filled polyamide 12 fabricated via FDM 3D printer for potential craniofacial reconstruction application. Castro et al. [16] developed a new kind of high permittivity (high-k) and low-loss composite material for fused deposition modeling (FDM) technology based on a cyclo olefin polymer (COP) thermoplastic matrix embedded with sintered ceramic. The cost of FDM technology is lower than other 3D printing technology, but its nozzle extrusion material molding method limits its molding speed, accuracy and the nozzle is easy to plug. Stereolithography (SLA) is a 3D printing technique based on curing a photopolymer with a UV laser or another similar power source and is known for its high accuracy and excellent surface finishing

[16–21]. Ceramic parts with complex 3D shapes can be manufactured using this method by mixing the ceramic powder and the photopolymer together analogously to the colloidal processing of ceramic powders. Digital light processing (DLP) is a new type of 3D printing technology emerging in recent years [22–25]. It is evolved from SLA. When the product is processed, the cross section of product is projected onto the surface of the liquid photopolymer by means of the digital micromirror element, so that the irradiated photopolymer is solidified layer by layer. DLP 3D printing is faster than the same type of SLA because it is layer-like solidification. The residual stress of samples prepared by DLP is small. This technique is ideal for high resolution prototyping.

In this study, HA ceramic parts were printed by homemade DLP 3D printing machine. The evaluation of the sintering process parameters and the mechanical properties of the scaffold were investigated. The biocompatibility of the HA scaffold was tested. The results suggest the printed ceramics with good compressive properties and biocompatibility through our homemade DLP 3D printer.

Materials and methods

Synthesis of bioceramic powders

A nano-sized HA powder with an average particle size of 20 nm was used in this study. The polymer was DSM's Somos® WaterShed XC 11122, which is a low-viscosity liquid photopolymer that produces strong, tough, water-resistant, ABS-like parts. In order to confirm the optimum concentrations of the HA power and polymer binder, different HA power concentrations (10, 20, 30, 40, 45 wt%) were prepared. The HA powder was added to the polymer to form the ceramic suspension. The ceramic suspension was then ball-milled for 12 h using zirconia balls. Figure 1a shows the viscosity of ceramic suspensions with different HA mass fractions. It could be seen that the fluidity of the ceramic suspension spread itself naturally in the groove when the HA concentration was between 0 and 30 wt%, but the spreading area decreased with the increase of the HA concentration; when the mass fraction of HA exceeded 30 wt%, the viscosity of the ceramic suspension rose rapidly. The mixture of HA mass fraction of 40 and 45 wt% could not be spread naturally in the groove.
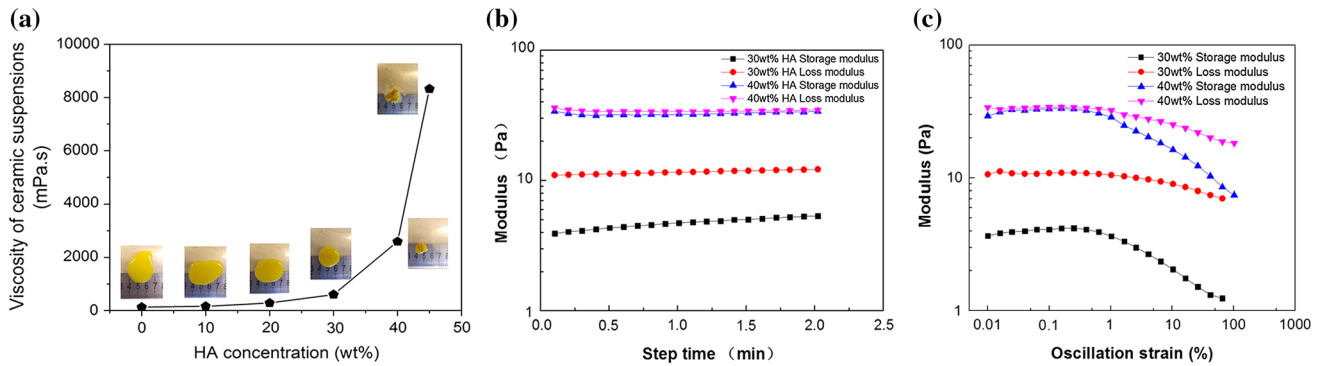
Figure 1 a The viscosity for ceramic suspensions as a function of different HA concentration fractions, the storage modulus and loss modulus as a function of **b** time and **c** strain for 30 and 40 wt% HA ceramic suspensions, respectively.

Figure 1b shows the storage modulus and loss modulus as a function of time for 30 and 40 wt% HA ceramic suspensions, respectively. The test temperature was room temperature, and the test time was 2 min. The frequency was 1 Hz, and the change in strain was within the linear viscoelastic region of the ceramic suspensions. It was clearly seen that the loss modulus was much larger than the storage modulus for the 30 wt% sample, which indicated that the 30 wt% HA ceramic suspension had a good fluidity. In comparison, the storage modulus and loss modulus of the 40 wt% sample were almost equal, which revealed that the 40 wt% HA ceramic suspensions were in a semisolid state. The poor fluidity of 40 wt% sample would cause the suspension cannot cover with the entire resin tank in the process of surface exposure. This was very detrimental to the quality of the print. In addition, it could be seen that the storage modulus and loss modulus of these two kinds of hydroxyapatite ceramic suspensions changed a little in 2 min, which indicated that the rheological parameters of the ceramic slurries were very stable. The suspension could maintain good fluidity and stability in the printing process. Figure 1c shows the storage modulus and loss modulus as a function of strain for 30 and 40 wt% HA ceramic suspensions, respectively. The test temperature was room temperature, the frequency was 1 Hz, and the strain range was 0.01 ~ 100%. Similar to Fig. 1b, it could be clearly seen that the loss modulus was much larger than the storage modulus for the 30 wt% sample. With the gradual increase of strain, the value of storage modulus decreased rapidly, which revealed that the fluidity of 30 wt% HA ceramic suspension became better as the strain became larger. On the other hand, the storage modulus and loss modulus of

40 wt% ceramic suspension did not change obviously in the range of 0.01 ~ 1%. When the strain value exceeded 1%, the storage modulus and loss modulus of 40 wt% HA ceramic suspension decreased. Similar to the 30 wt% sample, the loss modulus decreased faster than the storage modulus. This also indicated that as the strain increased, the fluidity of 40 wt% ceramic suspension became better. Under the same strain condition, the storage modulus increased with the increase of HA filling amount. The suspension was mainly composed of photosensitive resin and nanoceramic powder. The more the ceramic powder was filled, the more the solid content of the suspension was formed and the larger storage modulus of the suspension. As the strain rate increased, the influence of Penn effect gradually increased, and the storage modulus of the ceramic suspension decreased greatly.

So a ceramic suspension with HA mass fraction of 30 wt% was selected as the molding material in this experiment. Minimum essential medium alpha (α-MEM) and trypsin–ethylenediaminetetraacetic acid were purchased from Gibco. Dulbecco's phosphate-buffered saline (PBS) was purchased from Dycent Biotech (Shanghai) Co., Ltd. Bovine serum albumin, Triton X-100 and ascorbic acid were purchased from Sigma. The osteogenic medium used in this study comprised of α-MEM containing 10% fetal bovine serum (FBS, Atlas Biologicals), 1% penicillin–streptomycin (Lonza), 10 mM β-glycerol phosphate disodium salt hydrate (Calbiochem) and 50 μg/mL ascorbic acid. Deionized distilled water was produced by an ultrapure water system. All reagents and chemicals in this study were used without any further purification.

Preparation of HA scaffold

HA scaffold with square pore structure were prepared by using our homemade 3D printing equipment which named LAYING II 1510P. Figure 2a shows the mechanical structure of 3D printing machine. Settings were a layer height of 0.05 mm, a print speed of 20 mm/s. The ceramic suspension was poured into the transparent photopolymer trough, and a 21 mm × 21 mm × 3 mm mesh square three-dimensional model was designed by computer-aided design software. When the fabrication process was completed, the sample was dried at 85 °C for 3 h to remove excess water from the HA scaffold. Figure 2b shows the as-printed sample.

Scaffold sintering

On the one hand, the formed HA scaffold contains photosensitive polymer which needs to be removed; on the other hand, the mechanical property of the scaffold needs to be strengthened. So two-step sintering (TSS) was conducted. The TSS was performed in two heating regimes: (I) Heat treatment was employed to remove the polymer. In the removing polymer process, the regulation of rising rate of sintering temperature was very important. If the heating temperature rose too quickly, which would cause stress and affect the performance of the sample. And excessive heat might cause the carbonization of organic matter. Differential scanning calorimetry (DSC) and thermal gravity analysis (TG) were used to determine the sintering parameters. As can be seen from Fig. 3, with the increase of temperature, the quality of the sample began to decrease slowly. At the temperature from 300 to 500 °C, the weight loss changed most obviously, the quality of sample decreased by nearly 70%. And the quality did not change after 500 °C. According to the configuration proportion, the weight loss part should be photosensitive polymer, which would be decomposed at 500 °C. Seen from the DSC curve, the exothermic change was small from the room temperature to 300 °C. There were two larger endothermic peaks between 300 and 500 °C, which was the main decomposition reaction temperature range. According to the TG and DSC curves, the sintering parameters were determined. The temperature was kept unchanged for 10 min when the temperature reached 100 °C, which was to remove moisture from the sample. After that, the sample was fired up to 150 °C with heating rate of 1 °C/min and held for 10 min. At last, the sample temperature was increased to 500 °C at a rate of about 1 °C/min and held for 10 min. And (II) then the sample was heated up to 1200 °C with heating rate of 10 °C/min and held for 2 h. In the last, the sample was naturally cooled to room temperature. The second step sintering was to improve the crystalline quality of sample. Figure 2c shows the as-sintered sample.

Biocompatibility detection

In the clinical repair of bone defects, the HA scaffold needs to provide the site for osteoblasts to adhere, grow, proliferate and differentiate. Therefore, it is necessary to evaluate the biocompatibility of HA scaffold through biological cell culture experiments. MC3T3-E1 (newborn mouse-derived calvaria) cells were cultured in α-MEM supplemented with 10%
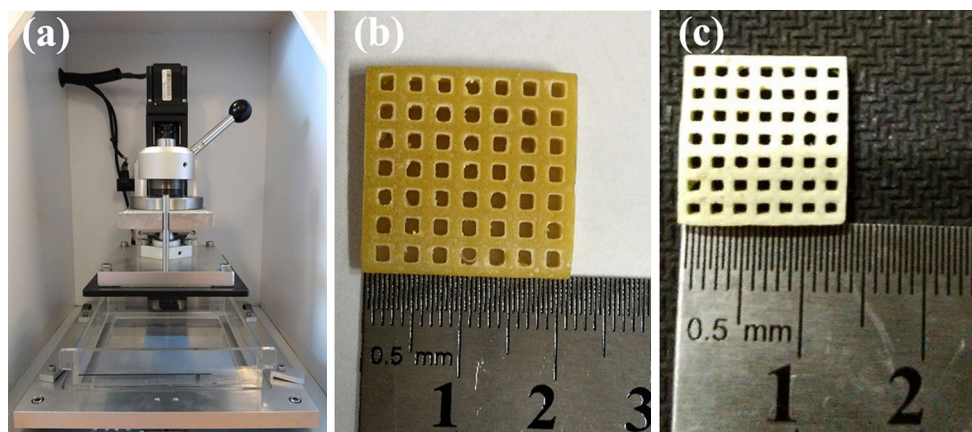
Figure 2 **a** The mechanical structure of 3D printing machine. **b** The as-printed sample. **c** The as-sintered sample.
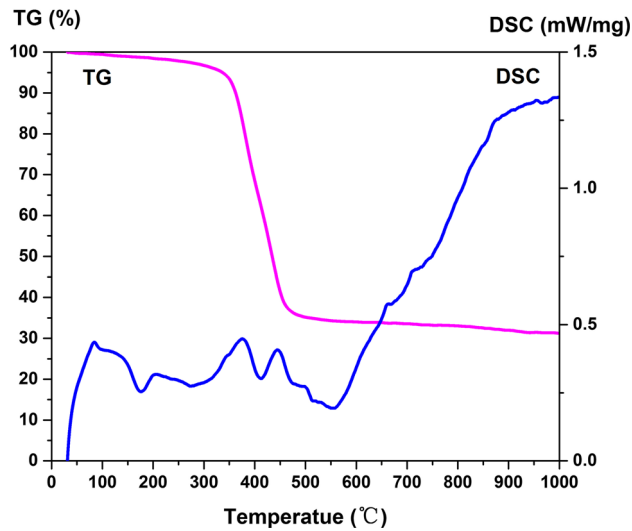
Figure 3 TG/DSC curves of the as-printed sample.

FBS and 1% penicillin streptomycin, and kept at 37 °C in a saturated humid atmosphere containing 95% air and 5% CO_2. Before cell seeding, the non-sterile samples were sterilized by ultra violet light for 1 h. The sterilized 3D scaffolds were placed in 96-well culture plates, and the cell suspension was added to the top center surface of the scaffolds, avoiding contact with the sides of the wells to improve seeding efficiency. After 3 h, the scaffolds were transferred to another 96-well culture plate and each of the wells was filled with 500 μL of fresh medium. The proliferation of the MC3T3-E1 cells on

Results

Dimensional shrinkage analysis

Figure 2b, c shows the as-printed and as-sintered sample, respectively. It can be seen that the size error of the as-printed sample and design model is small. The length and thickness of as-printed sample were 21.1 and 2.9 mm, respectively. The volume of as-printed sample was about 1291 mm^3. The size of as-sintered sample was slightly smaller. The length and thickness of as-sintered sample were 13.4 and 2.5 mm, respectively. The volume of as-sintered sample was about 449 mm^3. The shrinkage of the X–Y direction could be described: $S_{x-y} = \{(21.1 - 13.4)/21.1\} \times 100\% = 36.5\%$. The shrinkage of the Z direction could be described: $S_z = \{(2.9 - 2.5)/2.9\} \times 100\% = 13.8\%$.

DLP 3D printing parts were formed by stacking. In the curing process, the fluidity of the liquid slurry decreased significantly, and the change of solidification volume would cause shrinkage stress in the curing layer. The solidified scaffold belongs to the polymer composite material before the sintering process and can be regarded as an ideal elastic solid before its deformation reaches the yield limit. The element of the solidified scaffold has three orthogonal elastic symmetrical planes, which are orthotropic materials and have strain stress relations of orthotropic materials. The strain stress relation of the curing element can be expressed as:

$$
\begin{bmatrix} \varepsilon_x \\ \varepsilon_y \\ \varepsilon_z \\ \gamma_{yz} \\ \gamma_{zx} \\ \gamma_{xy} \end{bmatrix} = \begin{bmatrix} 1/E_x & -\mu_{yx}/E_y & -\mu_{zx}/E_z & 0 & 0 & 0 \\ -\mu_{xy}/E_x & 1/E_y & -\mu_{zy}/E_z & 0 & 0 & 0 \\ -\mu_{xz}/E_x & -\mu_{yz}/E_y & 1/E_z & 0 & 0 & 0 \\ 0 & 0 & 0 & 2(1+\mu_{yz})/E_{yz} & 0 & 0 \\ 0 & 0 & 0 & 0 & 2(1+\mu_{zx})/E_{zx} & 0 \\ 0 & 0 & 0 & 0 & 0 & 2(1+\mu_{xy})/E_{xy} \end{bmatrix} \begin{bmatrix} \sigma_x \\ \sigma_y \\ \sigma_z \\ \tau_{yz} \\ \tau_{zx} \\ \tau_{xy} \end{bmatrix} \quad (1)
$$

samples was determined. On the samples, 5000 cells/well were seeded and incubated for 12, 24, 36 and 48 h.

where ε_x, ε_y, ε_z, γ_{yz}, γ_{zx}, γ_{xy} are the positive strains and shear strains in three directions of X, Y and Z, respectively. $E_i(i = x, y, z)$ is the modulus of elasticity along the i direction. $E_{ij}(i, j = x, y, z)$ is the elastic

modulus between the i and j directions. $\mu_{ij}(i,j = x,y,z)$ is the Poisson ratio of the i direction that causes the deformation of the j direction. Since the thickness of the single curing layer is 0.05 mm, the curing size of the Z direction is much smaller than the curing dimension of X and Y. So a single cure layer can be considered as a plane strain problem. Therefore, $\varepsilon_z = 0$, $\gamma_{yz} = 0$, and $\gamma_{zx} = 0$. The stress–strain relation of a single curing layer can be expressed as:

$$\begin{bmatrix} \varepsilon_x \\ \varepsilon_y \\ \gamma_{xy} \end{bmatrix} = \begin{bmatrix} 1/E_x & -\mu_{yx}/E_x & 0 \\ -\mu_{xy}/E_x & 1/E_y & 0 \\ 0 & 0 & 2(1+\mu_{xy})/E_{xy} \end{bmatrix} \begin{bmatrix} \sigma_x \\ \sigma_y \\ \tau_{xy} \end{bmatrix} \tag{2}$$

In orthotropic elastic material, the coefficient of flexibility is $S_{ij} = S_{ji}(i,j = 1,2,3,\ldots,6)$. From Eq. (2) can be obtained:

$$-\frac{\mu_{xy}}{E_x} = -\frac{\mu_{yx}}{E_y} \tag{3}$$

In the surface exposure process, the curing layer is formed once for the exposure printing. The curing layer has the same effect on the deformation of each other in the direction of X and Y. That is, $\mu_{xy} = \mu_{yz}$ and $E_x = E_y$. It can be concluded that the surface forming solidification layer is uniformly contracted in the plane.

When the as-printed sample is sintered, the temperature of each part of the object changes. The sample will cause line strain $\alpha(\phi - \phi_0)$ due to thermal deformation. Where α is the coefficient of linear expansion of materials, ϕ is the instantaneous temperature value in any part of the elastomer, and ϕ_0 is the initial temperature value. In the three-dimensional problem, the temperature change caused by the temperature strain is:

$$\varepsilon_0 = \alpha(\phi - \phi_0)[1 \quad 1 \quad 1 \quad 0 \quad 0 \quad 0]^T \tag{4}$$

Then the load vector P of the object includes the volume load P_b and the surface load P_s, as well as the temperature load P_0 caused by the temperature strain:

$$P = P_b + P_s + P_0 \tag{5}$$

where

$$P_0 = \sum_e \int_{\Omega^e} B^T D \varepsilon_0 \, d\Omega \tag{6}$$

It can be seen from the above, compared with the stress analysis without thermal load problem, the structural thermal stress problem increases the temperature load term. In the sintering process, a slow heating rate can make the object heat tends to uniform. The heat shrinkage of the object under normal pressure sintering is not constrained, and the object is deformed without causing stress. The stress shrinkage of the material during the sintering process is similar to that of the curing layer, that is, the sintered part is also uniformly contracted in the plane. From the calculation results we can see that the shrinkage of the as-annealed sample in the X–Y direction is larger which in the Z direction.

Primary characterization of the sample

Figure 4 presents the XRD spectra of the HA scaffold. Peaks for standard phase pure HA (JCPDS # 09–0432) were observed in as-sintered sample. The black line was the XRD curve of sample which was processed after the first step of sintering, and the highest sintering temperature is 500 °C. As seen from the curve, there was no characteristic peak of other substances except the characteristic diffraction peaks of HA, which meant that the sample was pure phase after the first step sintering. The red line was the XRD curve of sample which was annealed after the second step of sintering, and the highest sintering temperature was 1250 °C. It could be seen from the red curve that the FWHM of HA peak was narrower and the
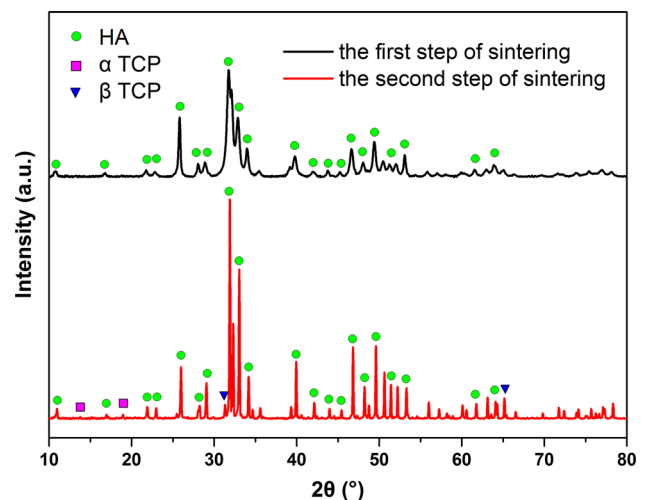
Figure 4 XRD of as-sintered HA sample.
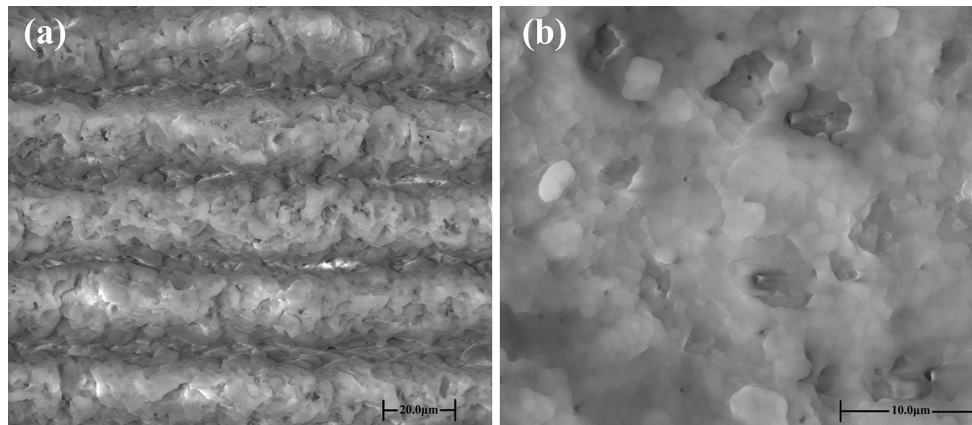
Figure 5 **a** Cross-sectional SEM morphology of the HA scaffold. **b** SEM image of the microstructure of as-sintered HA sample.

peak intensity was greater. It meant that HA had better crystalline quality after the second step of sintering. At the same time, a portion of HA was converted to tricalcium phosphate (TCP), including α-TCP and β-TCP. The α-TCP peaks were due to high-temperature phase transformation from β to α. Both HA and TCP are calcium phosphate bioceramics which have good biocompatibility, especially HA and β-TCP. There are some differences between the biological properties of these two substances. The HA has osteogenic effect, but its solubility in the human body is small; β-TCP has biodegradability, it can be gradually dissolved by new bone substitution in the human body.

Figure 5a shows the cross-sectional morphology of the as-sintered HA scaffold. It could be seen that the cross section had the layered structure formed by the exposure process, and the thickness parameters of the forming layer were 0.05 mm. Figure 5b shows the SEM image of the microstructure of the HA sample. As could be seen from the diagram the obvious grain boundary was found. There were no large and continuous pores in the cross section. There were no visible cracks. This showed that the sintered ceramics had a good crystalline quality.

## Compressive strength of the bioceramic scaffold

Compressive strength of the bioceramic scaffold is an important index to evaluate the performance of scaffold. The determination of compressive strength is generally axial compression, and the sample resists the pressure applied to the axial line. Brittle fracture and fragmentation will occur when the compressive

strength exceeds the compressive strength. Test specimen is usually cubes. In order to determine the structure of the compressive test specimens, three different test specimens were designed. Model 1, Model 2 and Model 3 are shown in Fig. 6a, b, c, respectively. Finite element simulation software is used to analyze the force of the three structures, and the C3D10 unit is used to mesh the model. The pressure of 12 MPa is applied on each sample surface. Figure 6d, e, f shows the result of the simulation.

It could be seen from the simulation results that both Model 2 and Model 3 had serious deformation, while Model 1 hardly deformed. From the distribution of the stress range, the stress concentration of Model 1 was the point distribution, which was distributed at the four corners of the bottom of the model. The stress of Model 2 was concentrated on the inclined support column of the model, and the area was large. The stresses of Model 3 were concentrated at the top of the beam, the supporting beam and their junction. From the magnitude of stress, the stress maximum of Model 1, Model 2 and Model 3 were 22.42, 26.65 and 38.28 MPa, respectively. Comprehensive analysis of the simulation results of the three models, the stress concentration phenomenon of Model 1 is the least obvious, and the maximum stress value was very small. Therefore, the structure of Model 1 was chosen to prepare the sample for compression test.

The samples were printed in use of LAYING II 1510P. Figure 6g shows the degreased cube sample which was used for compression testing. The formula for calculating compressive strength is described as:

$$P = \frac{F}{A} \tag{7}$$
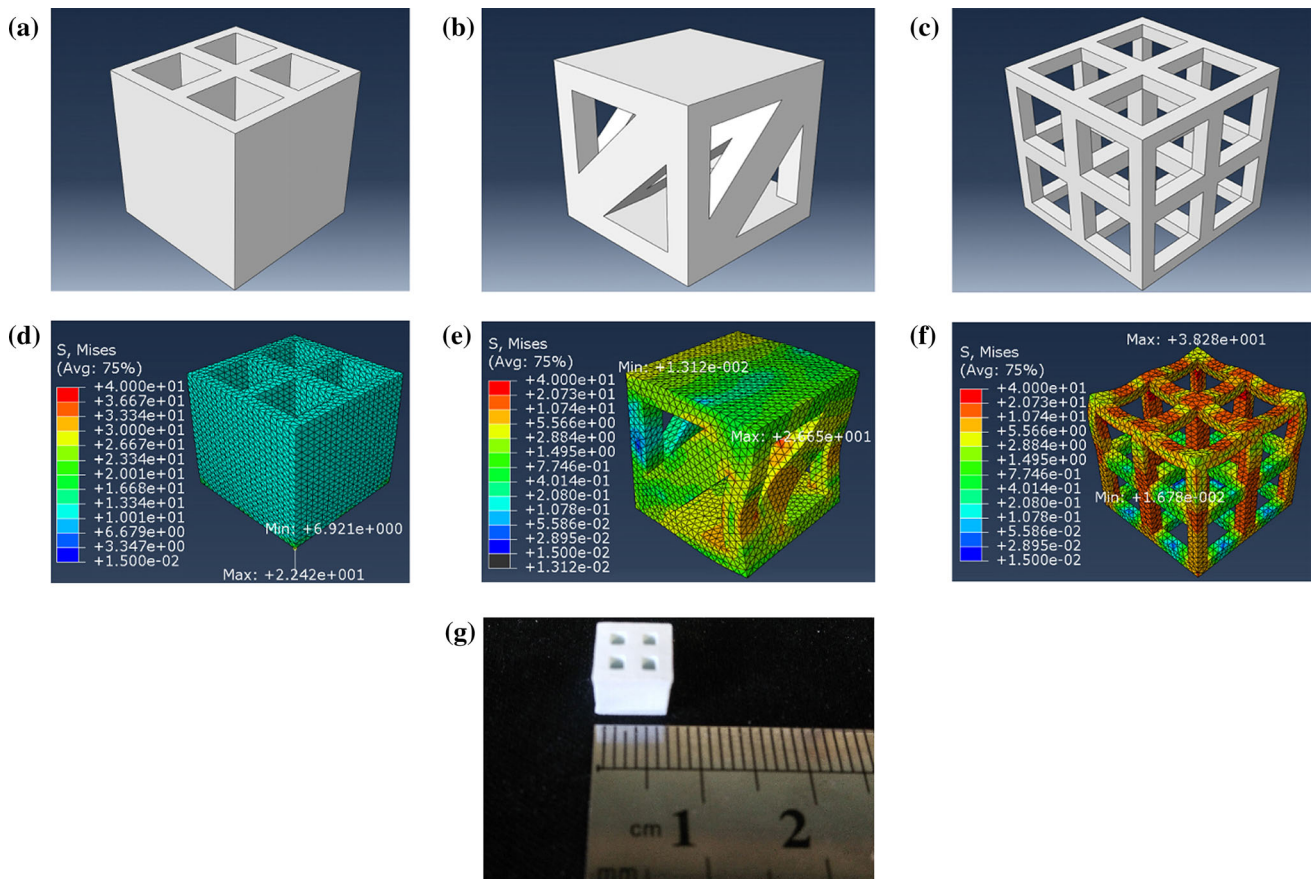
Figure 6 The compressive test specimens of **a** Model 1, **b** Model 2, **c** Model 3, respectively. The compression simulation results of **d** Model 1, **e** Model 2, **f** Model 3, respectively. **g** The degreased cube sample which was used for compression testing.
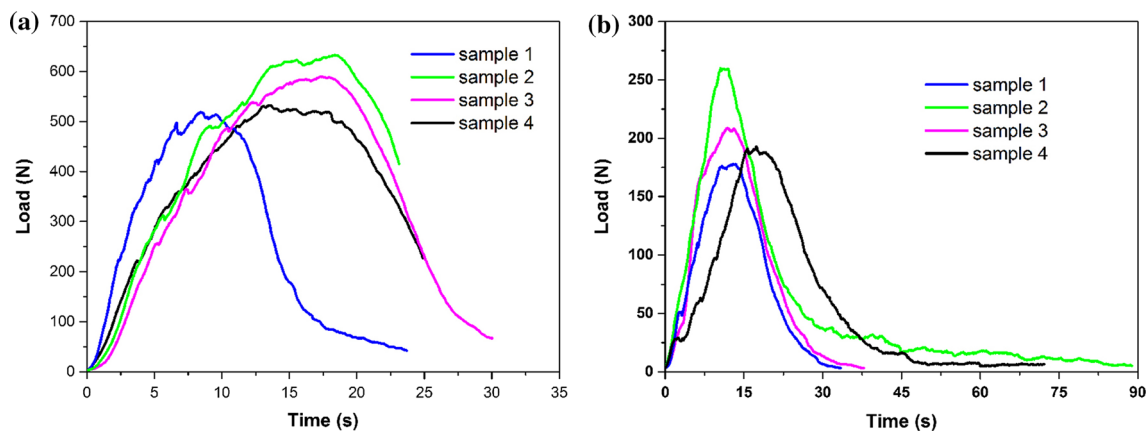
Figure 7 The test curve of the compressive strength in the **a** vertical and **b** horizontal direction of HA scaffolds.

where P is the compressive strength, F is the maximum load when the sample is damaged, A is the compression area. The electronic universal testing machine (CMT4304, MTS Systems Co. Ltd) was used to test the mechanical property. The speed was set to 1 mm/min. To ensure the accuracy of the data, four samples were tested in both vertical and horizontal directions, respectively. Figure 7a, b shows the load–time curve. According to the measured compressive area and the maximum load at break, the compressive strength of each sample was calculated (see Table 1). It could be seen that the compressive

Table 1 Test data of compressive strength of HA scaffolds

| Sample	Vertical direction			Horizontal direction		
	Compression area A (mm^2)	Maximum load F (N)	Compressive strength P (MPa)	Compression area A (mm^2)	Maximum load F (N)	Compressive strength P (MPa)
1	46.2	518.8	11.2	41.1	178.5	4.3
2	49.4	632.7	12.8	41.5	260.5	6.3
3	47.7	589.7	12.4	40.8	208.9	5.1
4	48.6	529.1	10.9	40.9	192.9	4.7

strength of the HA scaffold was high in the vertical direction. The compressive strength of each sample was more than 10 MPa, and the average value was 11.8 MPa. Compared with the compressive strength in the vertical direction, the compressive strength of the HA scaffold in horizontal direction was lower than 10 MPa, with an average value of 5.1 MPa. The results show that the HA scaffold printed by DLP has obvious anisotropy, and the strength of vertical direction is obviously better than that of horizontal direction. In the practical application, the corresponding repair structures should be constructed with the same strength-oriented bone tissue.

In vitro preosteoblast evaluation

In vitro studies were performed to evaluate the biological response of MC3T3-E1 cells grown on the scaffolds. Cell adhesive interactions play a critical role in preosteoblast survival, proliferation, differentiation and bone mineralization. We observed the initial adhesion of MC3T3-E1 cells cultured on scaffolds for 24 h. As shown in Fig. 8a, the cells adhered to the scaffold surface and spread well. This was beneficial for the growth of osteoblasts on the scaffold surface. The MC3T3-E1 cell proliferation on scaffolds

was determined by an MTT assay after being cultured for 12, 24, 36 and 48 h, as shown in Fig. 8b. It could be seen that the number of cells on HA scaffold increased significantly with the increase of time. A light microscope with 200-fold magnification was used to observe the macroscopic morphology of the MC3T-E1 cells on the scaffold. The result was shown in Fig. 8c. The elongated leaf-shaped dimples were the surface topography of the print, and the transparent raised objects were MC3T-E1 cells as shown in Fig. 8c. These cells were evenly and densely dispersed in a Petri dish. The adhesion of MC3T-E1 cells to the scaffolds was good, no large-scale death occurred.

An indirect immunofluorescence assay was used to test cell survival. Figure 9a shows the cell distribution of MC3T3-E1 before culture experiments. Figure 9b shows the cell distribution of MC3T3-E1 after 24-h culture. In this experiment, intracellular antibodies were labeled with fluorophores. Then these intracellular antibodies became fluorescent antibodies. Finally, the cells with fluorescent antibodies would be observed under a fluorescence microscope. Therefore, a bright spot taken by the fluorescent microscope represented a cell. The bright spot was the position of the fluorescent antibody, which was
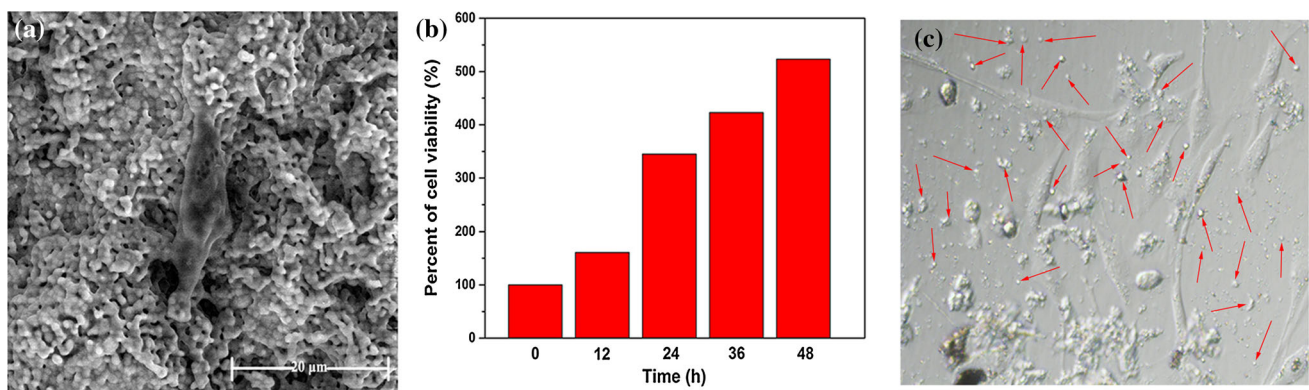
Figure 8 **a** SEM images of cells adhering to the scaffold surface. **b** Proliferation of cells. **c** Cell adhesion to the surface of the scaffold.
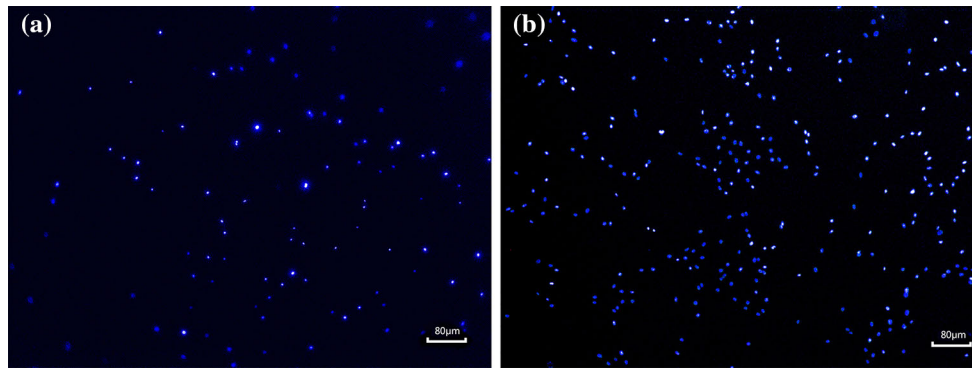
Figure 9 Fluorescence test of cells **a** before culture and **b** after 24-h culture, respectively.

also the location of the living cell. After a period of 24-h culture, the cells on the HA scaffold showed a wide range of proliferation, no large-scale death. The HA scaffolds provided MC3T3-E1 cells a good environment for proliferation, growth and adhesion. These results showed that the HA scaffold was biocompatible and suitable for cell growth and proliferation.

Conclusions

In summary, HA ceramics were printed by DLP in this study. The preparation of raw materials, the optimization of sintering process, the morphology of cross section, the phase composition and biocompatibility of as-sintered parts are studied in detail. The main conclusions are as follows: (1) HA powder and photopolymer were used as raw materials. When the powder quality ratio of HA was 30 wt%, the raw material not only had the characteristics of light curing, but also had good flow spreading property. It was suitable for DLP 3D printing technology and forming HA ceramic parts. (2) In the sintering process, the main temperature range of the decomposition reaction of the photopolymer was 300 $\sim$ 500 °C. In the process of photopolymer decomposition, controlling the heating rate could reduce the influence of the decomposition reaction and ensure the quality of the sintered parts. (3) After sintering, the shrinkage of the as-sintered sample in the $X–Y$ direction was larger, and the size of the Z direction was smaller. The shrinkage ratio of the sample in the forming direction of $X–Y$ was about 36.5%, the shrinkage in the Z direction was about 13.8%, and the volume shrinkage was about 65.2%. (4) After the sample was sintered, the photopolymer could be removed, and the calcium

phosphate ceramic phase could be obtained. The phase composition mainly consists of HA and β-TCP with good biological properties. (5) The biological properties of the scaffold were determined by cell culture in vitro. According to the proliferation of cells, it was concluded that the HA scaffold was biocompatible and suitable for cell growth and proliferation. The adhesion of the cell to the scaffold was observed, and it was confirmed that the scaffold was well integrated with the cell and was conducive to the migration and growth of the cells on the scaffold.

Acknowledgements

References

[1] Farag MM et al (2014) Effect of gelatin addition on fabrication of magnesium phosphate-based scaffolds prepared by additive manufacturing system. Mater Lett 132:111–115

[2] Rodriguez G et al (2013) Influence of hydroxyapatite on extruded 3D scaffolds. Procedia Eng 59:263–269

[3] Zein I et al (2002) Fabrication of 3D chitosan–hydroxyapatite scaffolds using a robotic dispensing system. Biomaterials 23:1169–1185

[4] Roh HS et al (2017) Addition of MgO nanoparticles and plasma surface treatment of three-dimensional printed polycaprolactone/hydroxyapatite scaffolds for improving bone regeneration. Mater Sci Eng C-Mater 74:525–535

[5] Wu HD et al (2016) Effect of the particle size and the debinding process on the density of alumina ceramics fabricated by 3D printing based on stereolithography. Ceram Int 42:17290–17294

[6] Slots C (2017) Andersendental, Simple additive manufacturing of an osteoconductive ceramic using suspension melt extrusion. Dent Mater 33:198–208

[7] Bendtsen ST et al (2017) Development of a novel alginate-polyvinyl alcohol-hydroxyapatite hydrogel for 3D bioprinting bone tissue engineered scaffolds. J Biomed Mater Res Part A 105:1457–1468

[8] Jakus AE et al (2017) Multi and mixed 3D-printing of graphene-hydroxyapatite hybrid materials for complex tissue engineering. J Biomed Mater Res Part A 105:274–283

[9] Lee JS et al (2016) Development and analysis of three-dimensional (3D) printed biomimetic ceramic. Int J Precis Eng Manuf 17:1711–1719

[10] Li X et al (2017) Biocompatibility and physicochemical characteristics of poly(ε-caprolactone)/poly(lactide-co-glycolide)/nano-hydroxyapatite composite scaffolds for bone tissue engineering. Mater Design 114:149–160

[11] Tian X et al (2009) Process parameters analysis of direct laser sintering and post treatment of porcelain components using Taguchi's method. J Eur Ceram Soc 29:1903–1915

[12] Muehler T et al (2015) Slurry-based additive manufacturing of ceramics. Int J Appl Ceram Technol 12:18–25

[13] Yen HC (2015) Experimental studying on development of slurry-layer casting system for additive manufacturing of ceramics. Int J Adv Manuf Technol 77:915–925

[14] Tang HH et al (2015) Slurry-based additive manufacturing of ceramic parts by selective laser burn-out. J Eur Ceram Soc 35:981–987

[15] Abdullah AM et al (2017) Mechanical and physical properties of highly ZrO_2/β-TCP filled polyamide 12 prepared via fused deposition modelling (FDM) 3D printer for potential craniofacial reconstruction application. Mater Lett 189:307–309

[16] Castro J et al (2017) Fabrication, modeling, and application of ceramic-thermoplastic composites for fused deposition modeling of microwave components. IEEE Trans Microw Theory 65:2073–2084

[17] Zocca A et al (2015) Additive manufacturing of ceramics: issues, potentialities, and opportunities. J Am Ceram Soc 98:1983–2001

[18] Schwentenwein M et al (2015) Additive manufacturing of dense alumina ceramics. Int J Appl Ceram Technol 12:1–7

[19] Zanchetta ZE et al (2016) Stereolithography of SiOC ceramic microcomponents. Adv Mater 28:370–376

[20] Woodward DI et al (2015) Additively-manufactured piezoelectric devices. Phys Status Solidi A 212:2107–2113

[21] Song X et al (2015) Ceramic fabrication using mask-image-projection-based stereolithography integrated with tape-casting. J Manuf Process 20:456–464

[22] Zhou M et al (2016) Preparation of a defect-free alumina cutting tool via additive manufacturing based on stereolithography–Optimization of the drying and debinding processes. Ceram Int 42:11598–11602

[23] Celine AM et al (2016) Adding biomolecular recognition capability to 3D printed objects. Anal Chem 88:10767–10772

[24] Shao HF et al (2017) Bone regeneration in 3D printing bioactive ceramic scaffolds with improved tissue/material interface pore architecture in thin-wall bone defect. Biofabrication 9:025003

[25] Zhu W et al (2016) 3D printing of functional biomaterials for tissue engineering. Curr Opin Biotech 40:103–112